Hadi Nazaripoor, Charles R. Koch, and Subir Bhattacharjee. Electrical perturbations of ultrathin bilayers: Role of ionic conductive layer. *Langmuir*, 30(49):14734–14744, 2014. doi: 10.1021/la503839x. PMID: 25419880

Langmuir
Article
pubs.acs.org/Langmuir

Electrical Perturbations of Ultrathin Bilayers: Role of Ionic Conductive Layer

Hadi Nazaripoor,[†] Charles R. Koch,*[,†] and Subir Bhattacharjee[‡]

[†]Department of Mechanical Engineering, University of Alberta, Edmonton, Alberta T6G 2R3, Canada
[‡]Water Planet Engineering, 721 Glasgow Ave, Unit D, Inglewood, California 90301, United States

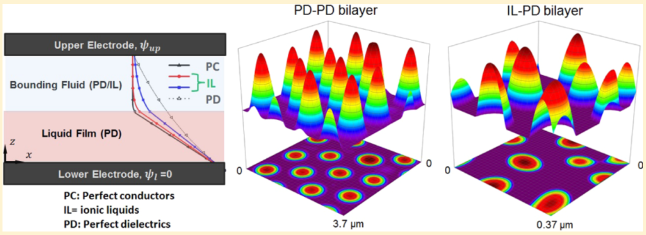

ABSTRACT: The effect of electrostatic forces on the dynamics, morphological evolution, and drainage time of ultrathin liquid bilayers (<100 nm) are investigated for perfect dielectric−perfect dielectric (PD−PD) and ionic liquid−perfect dielectric (IL−PD) bilayers. The weakly nonlinear "thin film" equation is solved numerically to obtain spatiotemporal evolution of the liquid−liquid interface responses to transverse electric field. In order to predict the electrostatic component of conjoining/disjoining pressure acting on the interface for IL−PD bilayers, an analytical model is developed using the nonlinear Poisson-Boltzmann equation. It is found that IL−PD bilayers with electric permittivity ratio of layers (lower to top), ε_r, greater than one remain stable under an applied electric field. An extensive numerical study is carried out to generate a map based on ε_r and the initial mean thickness of the lower layer. This map is used to predict the formation of various structures on PD−PD bilayer interface and provides a baseline for unstable IL−PD bilayers. The use of an ionic liquid (IL) layer is found to reduce the size of the structures, but results in polydispersed and disordered pillars spread over the domain. The numerical predictions follow similar trend of experimental observation of Lau and Russel. (Lau, C. Y.; Russel, W. B. Fundamental Limitations on Ordered Electrohydrodynamic Patterning; *Macromolecules* **2011**, *44*, 7746−7751).

■ INTRODUCTION

Thin films and surfaces are commonly applied to decorative or protective coatings,[1] an intervening media in liquid−liquid emulsions,[2,3] and occur as a lubricant in the cornea of the eye.[4] In technological processes where the stability of thin films is important, numerous theoretical and experimental studies have been conducted to understand the factors that lead to the rupture of the thin films.[1−13] Thin films are unstable when the wavelength of fluctuations is larger than a critical value.[5] Perturbations can lead to a diverse range of dynamics ranging from stable films to ruptured films showing dry spots/or holes. This behavior is attributed to the intermolecular interactions which are typically not significant in bulk fluid dynamics.[6] A pressure balance at the free interface is used to determine the shape between the layers. Thin film instability can be triggered naturally[9,14,15] (i.e., intermolecular forces) and by externally applied forces[2,13,16−23] (i.e., mechanical, thermal, and electric forces). Films with thicknesses of 100 nm or less are called ultrathin films and can be either stable or unstable depending on the sign of the second derivative of the interaction potential with respect to film thickness.[5] Natural intermolecular interactions (such as van der Waals interactions, apolar,[5,8,24] and polar interactions[9]) determine the initial state of a thin film on a substrate. The type and magnitude of the interactions depend on properties of system materials.[25,26]

Applying an electric field can also cause film motion due to creation of a stress at the film interface. Electrically induced instability of thin films has received extensive attention as a tool for generating novel submicrometer structures,[16,19,20,27−31,31−45] with applications in the fabrication of microfluidic devices, biosensors, fuel and solar cells, and optoelectronic devices. Among several micro and nanofabrication methods (e.g., self-assembly, soft lithography, optical lithography, nanoimprinting, etc.), electrohydrodynamic lithography (EHL) is a promising technique to create micron and submicron patterns at the thin liquid/molten polymer film interface. This is due to the capability of EHL in generating complex structures rapidly and economically.[32] Raising the electric field above a critical value results in crease formation in the thin film and a further increase in the electric field can cause crater formation on the polymer interface.[19,43]

Electrohydrodynamic (EHD) pattern formation is an energy driven process[30] where the dynamics of structures (i.e., pillars, holes, and bicontinuous pattern formation) form to minimize the main energy component, the electrostatic energy. From a thermodynamic point of view, the film evolves to lower the free energy of system[29,30] such that at steady state the lowest interfacial energy determines the final structure.

Initial stages of film evolution can be described by linear stability (LS) analysis, whereas further stages show nonlinear behavior.[8,14,46] Feature size in the EHD process is characterized by the fastest growing wavelength of instabilities, $\lambda_{\max}$. The

Received: July 25, 2014
Revised: November 22, 2014

center-to-center distance of pillars in (typically a hexagonal pillar pattern) can be predicted by LS analysis.[16,27,29,32,39,41] In LS analysis, $\lambda_{\max}$ is a function of electric permittivity of layers ε, electrode distance d, initial mean film thickness h_0, applied voltage V, and interfacial tension γ.[16,27,29] Bilayers with $\varepsilon_r > 1$ have been widely studied both numerically[29,34,41,47,48] and experimentally;[16,27,31,33,35,39] bilayers with $\varepsilon_r < 1$ have received less attention despite their potential for producing smaller features as demonstrated by experiments.[27,39]

Dynamics and spatiotemporal evolution of perfect dielectric (PD) and leaky dielectric (LD) bilayers which are bounded with air are numerically modeled for both flat and patterned electrodes.[38,44] PD materials, with no free charge, polarize under the electric field, but in LD materials, with infinitesimal amount of charges, charges move and accumulate on the electrode surface and the interface.[49] Significant decrease in the length scale of structures is observed due to the presence of free charges at the interface.[44,50] It is experimentally shown that the use of an ionic liquid (IL) bounding layer results in submicrometer-sized features even with the use of flat electrodes.[39] Ionic liquids can be ionic salt like materials, considered as high temperature ionic liquids, or low temperature ionic liquids[39] which are liquid below 100 °C and electrolytes (aqueous or nonaqueous).[51]

An IL−PD interface which is subject to an applied electric field is present in many microfluidic system applications. Free ions present in the ionic liquids and under the applied electric field redistribute and accumulate on the charged surfaces. The diffuse layer of ions is called the electric double layer (EDL). The EDL structure is essential to obtain the electromechanical behavior of IL−PD interface.[51,52] This diffuse layer is not present in perfect dielectrics and leaky dielectrics. Another difference is the electroneutrality condition of bulk in the leaky dielectric case.

Dynamics of the free ions within IL material is governed by the Poisson-Nernst-Planck equation which leads to the Boltzmann distribution for an equilibrium condition[51] where the charge relaxation time is much smaller than the process time.[26] It is observed that IL layers subjected to a strong electric field (over $O(10^8)$ V/m) behave like a perfect conductor.[52] Since the applied voltage and the upper layer thickness in the EHD patterning process result in the IL layer experiencing both strong and weak electric field conditions, a comprehensive electrostatic model is needed to predict both perfect conducting and EDL behavior of the IL layer.

An analytical model based on the coupled nonlinear Poisson-Boltzmann and Laplace equations to obtain the electric potential distribution within layers and consequently the electrostatic pressure acting on the interface is developed. Then, a comprehensive numerical investigation is performed to investigate the morphological behavior of bilayers. Layers with an electric permittivity ratio of less than one ($\varepsilon_r < 1$) under a homogeneous electric field are the focus of this investigation. The morphology of the film and its drainage time under the effects of filling ratio and electric permittivity ratio are studied. Finally, the perfect dielectric (PD) upper layer is replaced with an IL layer to investigate spatiotemporal behavior of the bilayer. Analytical calculations are performed and integrated into the numerical simulation to obtain the interface potential and to define an electrostatic component of conjoining/disjoining pressure acting on the interface.

■ PROBLEM FORMULATION

A schematic of the thin film sandwiched between upper and lower electrodes is shown in Figure 1a. Thin film evolution is described using mass and momentum conservation for both the thin film and the bounding fluid.

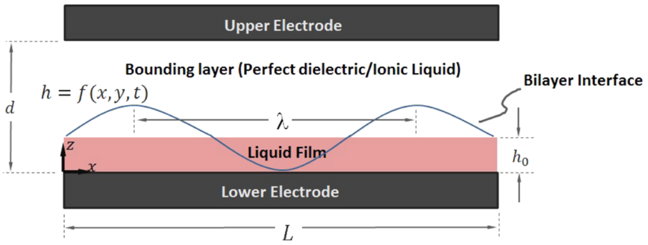

Figure 1. (a) Schematic view of the thin film sandwiched between electrodes. The z-position of the free interface is described by the function $h = f(x, y, t)$ with the lateral coordinates x, y, and time t. The amplitude of the fluctuation with wavelength is not to scale and is magnified. d = 100 nm.

$$\nabla.\, \vec{u}_i = 0 \tag{1}$$

$$\rho_i\left(\frac{\partial \vec{u}_i}{\partial t} + (\vec{u}_i.\, \nabla \vec{u}_i)\right) = -\nabla P_i + \nabla.\, [\mu_i(\nabla \vec{u}_i + (\nabla \vec{u}_i)^T)] + \vec{f}_e \tag{2}$$

These equations are solved with the following boundary conditions: no slip condition on the walls ($\vec{u}_i = 0$ *at* $z = 0$ and $z = d$), no penetration (two media are immiscible: $\vec{u}_{\text{relative}} = 0$) and stress balance (normal: $\vec{n}.[\overline{\sigma}_1.\vec{n} - \overline{\sigma}_2.\vec{n}] = \kappa\gamma + \vec{f}_e.\vec{n}$ and tangent: $\vec{t}_i.[\overline{\sigma}_1.\vec{n} - \overline{\sigma}_2.\vec{n}] = \vec{f}_e.\vec{t}_i$) at the interface ($z = h(x, y, t)$), where $\overline{\sigma} = -P\overline{I} + \mu_i(\nabla \vec{u}_i + (\nabla \vec{u}_i)^T)$ and $\vec{f}_e = -\nabla\phi$ is for external body force, ϕ is conjoining pressure, μ_i is the dynamic viscosity, and subscript i denotes the fluid phase (here 1 and 2 for the thin film and the bounding media, respectively). The normal and tangent vectors of the interface are $\vec{n}$ and $\vec{t}_i$, respectively.[53] The surface tension, γ, is assumed to be constant and κ is the mean interfacial curvature of the film interface.[53]

The liquid layers are assumed Newtonian, incompressible, and have an electric permittivity of $\varepsilon_1(\varepsilon_2)$ for lower (upper) layer. The film is assumed sufficiently thick that the continuum assumption is valid, but thin enough that gravity effects can be neglected. The system is assumed isothermal so energy conservation is not needed. A kinematic boundary condition is used to relate interfacial velocity component to the film thickness as[8]

$$w = \frac{\partial h}{\partial t} + u\frac{\partial h}{\partial x} + v\frac{\partial h}{\partial y} atz = h(x, y, t) \tag{3}$$

In the EHL process, an applied electric field destabilizes the interface of the liquid film and bounding fluid, leading to the evolution of patterns with height of $h = f(x, y, t)$. The wavelengths of the growing instabilities, λ, are much larger than the initial film thickness (at initial stages), so a "long-wave approximation"[10] is used to simplify the governing equations. Inertial effects are also negligible because the thickness of the lower layer remains less than 100−200 nm during the film dynamics, which leads to Reynolds number which is much smaller than one (Re < 1). To reduce the computational effort, the polymer film (lower layer) is assumed much more viscous than the bounding fluid (upper layer). Applying these assumptions to the governing equations and boundary conditions results in the following "thin film" equation:[12,24,29,41,54]

$$3\mu h_t + \frac{\partial}{\partial x}\left[h^3\frac{\partial\psi}{\partial x}\right] + \frac{\partial}{\partial y}\left[h^3\frac{\partial\psi}{\partial y}\right] = 0$$
$$\psi = \gamma[h_{xx} + h_{yy}] - \phi \tag{4}$$

which is a long-wave limit description of spatiotemporal evolution of film interface, $h(x, y, t)$. In ψ, $\gamma[h_{xx} + h_{yy}]$ is the surface tension force, while ϕ represents the excess intermolecular forces, which is a conjoining pressure as mentioned previously. Laplace pressure (the first term in ψ) is a result of local curvature of the free interface and interfacial tension. By minimizing the interface area of the film and the free energy of system, this term damps fluctuations.[25] The viscous term, $3\mu h_t$, also damps fluctuations in the fluid film. Increasing the films viscosity increases film evolution times.[55]

Interaction Potentials. Conjoining pressure, ϕ, (force acting on the film interface per unit area) is defined as the gradient of excess intermolecular interactions, $\phi = \nabla(\Delta G)$. In EHD, the electric field induces a pressure at the film interface which is added to the natural interactions to generate excess intermolecular interactions. The conjoining pressure, ϕ, is a summation of these interaction potentials: van der Waals, electrostatic, and Born repulsive interaction potentials and is given as

$$\phi = \phi_{\text{vdW}} + \phi_{\text{Br}} + \phi_{\text{EL}} \tag{5}$$

The van der Waals interaction is the summation of Keeson, Debye, and London dispersion forces.[25,26] This interaction is defined as $\phi_{\text{vdW}_\text{L}} = A_\text{L}/6\pi h^3$ and $\phi_{\text{vdW}_\text{U}} = -A_\text{U}/6\pi(d - h)^3$ for the lower and upper electrodes, respectively. A_L and A_U are effective Hamaker constants for the electrodes which depend on the materials used for electrodes and fluid layers.[25,26]

The van der Waals interaction are singular as $h \to 0$ and $h \to d$. To avoid nonphysical penetration of liquid to solid phase, in case of film rupture and touching, a cutoff distance, l_0, is defined for which a short-range repulsive force, called Born repulsion, acts on the film interface.[15,24,29,41] This is used to maintain a minimum equilibrium liquid thickness on both electrodes and is defined as $\phi_{\text{Br}_\text{L}} = -8B_\text{L}/h^9$ and $\phi_{\text{Br}_\text{U}} = 8B_\text{U}/(d - h)^9$ for the lower and upper electrodes, respectively. Coefficients B_L and B_U are found by setting the net conjoining pressure equal to zero at $h = l_0$ and $h = d - l_0$ for lower and upper surfaces. The most significant component of the conjoining pressure is the electrostatic pressure developed due to Maxwell stress[56]

$$\phi_{\text{EL}} = \frac{1}{2}\varepsilon_0\left[\varepsilon_1\left(\frac{\partial\psi_1}{\partial z}\Big|_{z=h}\right)^2 - \varepsilon_2\left(\frac{\partial\psi_2}{\partial z}\Big|_{z=h}\right)^2\right] \tag{6}$$

where ε_1 (ε_2) is the relative electric permittivity of lower (top) layer and ε_0 is free space electric permittivity. For the air−polymer bilayers (i.e., PD−PD materials with no free charge), the Laplace equation governs the electric potential in the layers.[16,29,41]

$$\varepsilon_i\varepsilon_0\nabla^2\psi_i = 0 \tag{7}$$

For the IL layer case, with N numbers of species in the electrolyte, the Poisson equation is used to obtain electric potential in the IL layer.

$$\varepsilon_i\varepsilon_0\nabla^2\psi_i = -\rho_f \tag{8}$$

The boundary conditions are the applied potential on the upper electrode, grounded for the lower electrode, and the electric displacement and potential continuity at the bilayer interface. In eq 8, ρ_f accounts for the free charge distribution within the IL layer which is related to the ionic number concentration as $\rho_f = \sum_{i=1}^{N}\overline{z}_i e n_i$. Free ions move and stay close to the charged surfaces to form a Debye layer.[26] The dynamics of the free ions become insignificant when using a Boltzmann distribution. The Boltzmann distribution must satisfy the electroneutrality condition within the IL layer and is derived from ion conservation equation in an equilibrium condition

$$n_i = n_{i\infty}\exp\left[-\frac{\overline{z}_i e(\psi - \psi_{\text{ref}})}{k_\text{B}T}\right] \tag{9}$$

where ψ_{ref} and $n_{i\infty}$ are reference potential and bulk ion number concentration, respectively. The reference potential ψ_{ref} is set as the applied voltage. For the ith species in the electrolyte, $\overline{z}_i$ is the valence, e is the magnitude of electron charge, k_B is the Boltzmann constant, and T is the temperature in K. Bulk ion number concentration depends on the molarity of electrolyte, $n_\infty = 1000N_\text{A}M$, for which N_A is the Avogadro number and M is the electrolyte molar concentration. The nondimensional electric potential and length are defined as $\Psi = ez\overline{\psi}/k_\text{B}T$ and $Z = z/(d - h)$, respectively. The nondimensional Laplace and nonlinear Poisson-Boltzmann equations in the long wave limit are

$$\frac{\text{d}^2\Psi_1}{\text{d}Z^2} = 0 \tag{10}$$

$$\frac{\text{d}^2\Psi_2}{\text{d}Z^2} = (\kappa(d - h))^2\sinh(\Psi_i - \Psi_{\text{ref}}) \tag{11}$$

These are solved to find electric potential distribution across the PD layer, $0 \le Z \le (h/(d - h))$

$$\Psi_1 = \left(\frac{d - h}{h}\right)\Psi_s Z \tag{12}$$

and the IL layer, $(h/(d - h)) \le Z \le (d/(d - h))$

$$\Psi_2 = \Psi_{\text{up}} + 2\ln\left[\frac{1 - \exp\left(\kappa(d - h)\left(\frac{h}{(d-h)} - Z\right)\right)\tanh\left\{\frac{(\Psi_{\text{up}} - \Psi_s)}{4}\right\}}{1 + \exp\left(\kappa(d - h)\left(\frac{h}{(d-h)} - Z\right)\right)\tanh\left\{\frac{(\Psi_{\text{up}} - \Psi_s)}{4}\right\}}\right] \tag{13}$$

where $\kappa = ((\varepsilon_2\varepsilon_0 k_\text{B}T)/(2e^2z^2n_\infty))^{1/2}$ is the inverse of Debye length.[26] The nondimensional interface electric potential, Ψ_s, can be found by solving the following nonlinear equation

$$\Psi_s - \frac{2\varepsilon_2\kappa h}{\varepsilon_1}\sinh\left(\frac{(\Psi_{\text{up}} - \Psi_s)}{2}\right) = 0 \tag{14}$$

It is assumed that the IL is a symmetric ($\overline{z}$: $\overline{z}$) and monovalent electrolyte. It should be noted that use of long wave approximation is valid for the early stages of film evolution. Linear stability (LS) analysis shows that using long wave limit approximation overestimate the maximum wavelength of instability growth when compared to a general model.[40,42] Using the electric potential distribution obtained from eqs 12 and 13 and combining with the electrostatic pressure in eq 6 results in a conjoining pressure acting on the IL−PD bilayer interface of

$$\phi_{\mathrm{EL}} = -\frac{1}{2}\varepsilon_1\varepsilon_0\left(\frac{\varepsilon_1}{\varepsilon_2} - 1\right)\left(\frac{\psi_s}{h}\right)^2 \qquad (15)$$

For bilayers that act like perfect dielectrics the electrostatic component of conjoining pressure is[29]

$$\phi_{\mathrm{EL}} = -\frac{1}{2}\varepsilon_1\varepsilon_0\left(\frac{\varepsilon_1}{\varepsilon_2} - 1\right)\left[\frac{\psi_{\mathrm{up}}}{h\left(1 - \frac{\varepsilon_1}{\varepsilon_2}\right) + \frac{\varepsilon_1}{\varepsilon_2}d}\right]^2 \qquad (16)$$

Linear Stability Analysis. To predict the characteristic wavelength for growth of instabilities, linear stability analysis has been performed for PD−PD bilayers[12,16,27,36,37,55,57] and PD−IL bilayers.[51] For a thin PD liquid film bounded with an IL layer, the LS analysis is found by substituting the interface height, h, in eq 4 with small sinusoidal perturbation of the interface, $h = h_0 + \xi \exp[i(k^*x + k^*y) + st]$ and neglecting the nonlinear terms. k^* is wavenumber, s is the growth coefficient, and ξ is the amplitude. The linear dispersion relation, s, and the resulting dominant wavenumber, $k^*_{\max}$, of the fastest growing wave are $s = -[({h_0}^3k^{*2})/(3\mu)][(\partial\phi/\partial h)|h_0 + k^{*2}\gamma]$ and $k^*_{\max} = \{[(\partial\phi/\partial h)|h_0]/(-2\gamma)\}^{1/2}$, respectively. The term $(\partial\phi/\partial h)|h_0$ represents the gradient of conjoining pressure with respect to the interface height evaluated at the initial film thickness. In the initial stages of EHD patterning, the electrostatic interaction is dominant; therefore, ϕ in κ^* and s is replaced with ϕ_{EL}.

Since the bilayer interface potential is a function of interface location, applied voltage, electric permittivity of layers, and the Debye length (eq 14), changing any of these parameters changes the interface potential and the electrostatic component of conjoining pressure and consequently the shape and size of the structures. For simulation, time ($T = t/t_s$) and length ($X = x/\lambda_{\max}$ and $Y = y/\lambda_{\max}$) are scaled using $t_s = 12\mu\gamma/h_0^3(\partial\phi_{\mathrm{EL}}/\partial h)^2$ and $\lambda_{\max} = 2\pi(k^*_{\max})^{-1}$ from LS analysis. The liquid film thickness is scaled to the mean initial thickness, $H = h/h_0$.

Numerical Method. To obtain transient behavior of the liquid−liquid interface, the governing equations (eqs 4 and 5) are solved numerically. Solution of this 4th order nonlinear partial differential equation (PDE) employs an adaptive time step ordinary differential equation (ODE) solver for the temporal and a finite difference method for the spatial direction. First, spatial derivatives are discretized using finite difference to convert the PDE to a differential algebraic equation (DAE) in time. Differential algebraic solver (DASSL) with an adaptive time stepping is then used for the DAE system.[58] A domain with length of $\lambda_{\max}$ or larger is sufficient to see the growth of instabilities when periodic boundary conditions are chosen; otherwise, fluctuations will damp out over time.[24] For notation simplicity, λ will be used instead of $\lambda_{\max}$. A square domain with size of $(4 \times 4)\lambda^2$ and a periodic boundary condition for both x and y directions are chosen. A uniform Cartesian grid is used throughout this study with 121 × 121 spatial grids. Initial conditions for the simulation are a random disturbance while maintaining liquid film volume. The simulation parameters and constants used in this study are listed in Table 1.

■ RESULTS AND DISCUSSION

The use of an external electric field induces instabilities on the deformable film interface to create a variety of structures from simple hexagonal ordered columns, the bicontinuous and holes[16,27−33,35,36,39,41,42,44,55] to the more complex ones such as cage-like,[59] hierarchical,[60] core−shell, and embedded[57] structures. The film interface structure changes under a homogeneous electric field based on the relative electric permittivity difference of layers which determines the net electric force direction. Referring to eq 16, for the case of $\varepsilon_1 > \varepsilon_2$ ($\varepsilon_1 < \varepsilon_2$) the electrostatic force acts upward (downward) which results in a disjoining (conjoining) pressure.

Table 1. Constants or Parameters Used in Simulations

parameter	value
electron charge magnitude (e)	1.602×10^{-19} C
Boltzmann constant (k_B)	1.378×10^{-23} J/K
Avogadro number (N_A)	6.022×10^{23} 1/mol
free space electric permittivity (ε_0)	8.85×10^{-12} C/V m
viscosity of liquid film (μ)	1 Pa s
effective Hamaker constant (A)	-1.5×10^{-21} J
interfacial tension (γ)	0.048 N/m
electric permittivity of the liquid film (ε_1)	2.5 (−)
electric permittivity of the bounding media (ε_2)	1−36 (−)
molarity (M)	0.01−1 mmol/L
initial film thickness (h_0)	20−85 nm
electrodes distance (d)	100 nm
Born repulsion cut off distance (l_0)	1−8 nm
applied voltage (ψ_{up})	0.25−70 V

In ionic liquids, migration and redistribution of free ions result in double layer formation close to the interface. This accumulation of ions alters the electric potential distribution within the IL layer and depends on the ionic strength which is characterized by the Debye length, k^{-1}. The conductivity of ionic liquids increases with high molarity and lower Debye length. The analytical solution, eqs 12 and 13, is examined for three values of molarity in the IL−PD bilayer and results are compared to the electric potential distribution in a PD−PD bilayer in Figure 2a. Electric permittivity ratio, $\varepsilon_r = 0.6$, and applied potential, $\phi_{\mathrm{up}} = 0.25$ V, are kept constant.

Ionic liquids with higher molarity, $M = 1$ mmol/L (lower Debye length $k^{-1} = 1.08$ nm) act like perfect conductors and electric potential decreases slightly near the interface, whereas a potential drop close to the interface is more significant when the ionic strength is lower, $M = 0.01$ mmol/L (higher Debye length, $k^{-1} = 10.8$ nm). For the PD film, as expected from solution of the Laplace equation, electric potential decreases linearly near zero at the lower electrode (see Figure 2a). The proposed analytical solution, eqs 13 and 14, gives reasonable results for ionic liquids with $M \geq 0.01$ mmol/L (i.e., $k^{-1} \leq 10.8$ nm). The maximum growth rate, $s_{\max}$, and its corresponding maximum wavenumber, $k^*_{\max}$ are found for IL−PD bilayers from LS analysis. Growth rates as a function of wavenumber for IL−PD and PD−PD bilayers are compared in Figure 2b. The maximum wavenumber is increased when the PD bounding layer is replaced with the IL one which results in lower maximum wavelength, $\lambda_{\max}$, resulting in smaller center to center distance of pillars.[16]

As shown in Figure 2a, higher ionic strength leads to lower electric potential drop within IL layer. Therefore, the lower layer film experience a higher electric field. Consequently a IL−PD interface is subject to higher electrostatic pressure, ϕ_{EL} (eq 15). Effects of electrolyte molarity on the net electrostatic pressure acting on the IL−PD interface for two electric permittivity ratio of layers, $\varepsilon_r = 0.6$ and 2.5, are shown in Figure 3a. In all cases, the magnitude of electrostatic pressure decays as the interface height increases. The negative values for ϕ_{EL} represent the upward disjoining pressure and positive values are downward conjoining pressure.

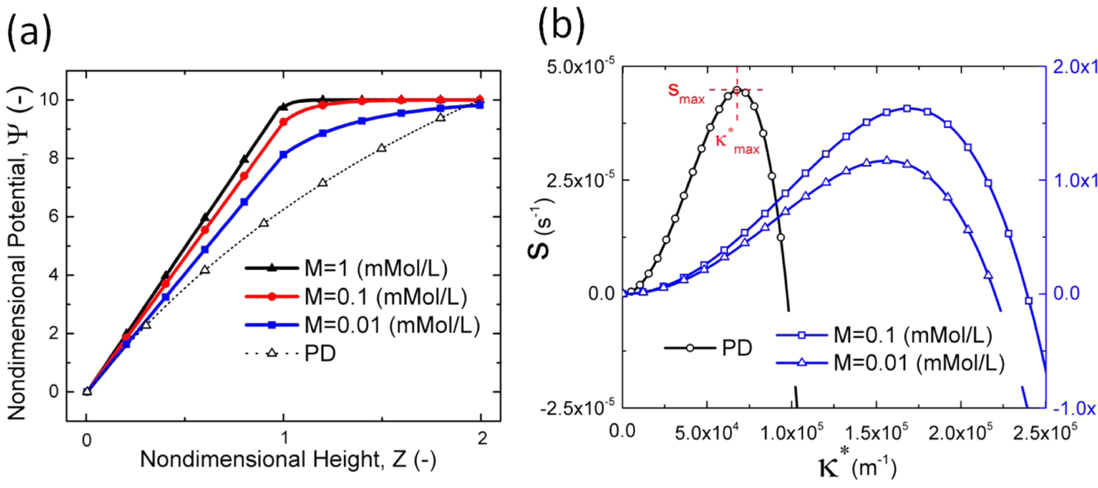

Figure 2. Effects of IL layer molarity on (a) nondimensional electric potential, $\Psi = e\psi/k_B T$, variations versus nondimensional height, $Z = z/(d - h)$ and (b) growth rate, s, variations versus wavenumber, k^*. $d = 100$ nm, $h_0 = 50$ nm, $\psi_{up} = 0.25$ V, $\varepsilon_1 = 2.5$, and $\varepsilon_2 = 4.17$.

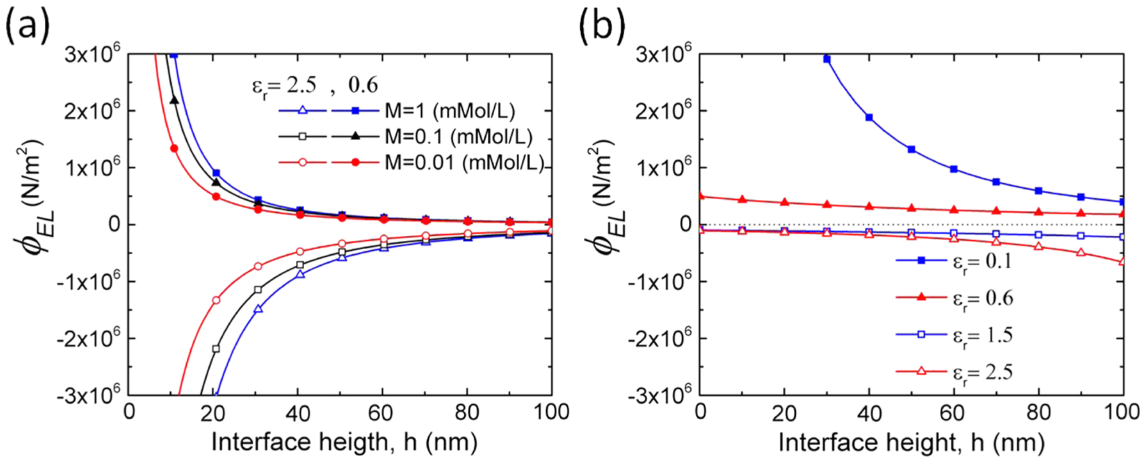

Figure 3. Electrostatic pressure variations versus interface height. Effects of (a) electrolyte molarity in IL−PD bilayers, (b) relative electric permittivity ratios of layers in PD−PD bilayers, ε_r. Applied potential, ψ_{up}, is (a) 0.25 and (b) 20 V and $\varepsilon_1 = 2.5$.

The effects of relative electric permittivity ratios of the fluid layers in PD−PD bilayers on the electrostatic conjoining/disjoining pressure is presented in Figure 3b. In this case the applied potential, $\psi_{up} = 20$ V, is 80 times greater than that used for the IL−PD bilayers (Figure 3a). Comparing ϕ_{EL} values for $\varepsilon_r = 0.6$ and 2.5 between IL−PD bilayers and PD−PD bilayers show that electrostatic pressure varies more uniformly with change of interface height in PD−PD bilayers. Using bounding layers with high relative electric permittivity in PD−PD bilayers also leads to higher electrostatic pressure with similar exponential decrease as a function of interface height to IL−PD bilayers. Although the applied potential is 80 times smaller in the IL−PD case, the interface experience higher electric pressure even without considering the change in molarity.

When the spinodal parameter (derivation of conjoining pressure with respect to the film thickness) becomes negative, the film becomes unstable. For the PD−PD bilayers (eq 16), both cases $\varepsilon_1 > \varepsilon_2$ and $\varepsilon_1 < \varepsilon_2$ result in negative spinodal parameter values. However, for the IL−PD bilayers (eq 15), the spinodal parameter is negative only for bilayers with $\varepsilon_1 < \varepsilon_2$. Therefore, this study focuses on the unstable case, where the upper layer has a higher electric permittivity than the lower layer ($\varepsilon_1 < \varepsilon_2$).

Variations in electrostatic pressure due to change in applied potential for PD−PD and IL−PD bilayers are presented in Figure 4. To show the broad range of variations in ϕ_{EL}, results are plotted on a log−log scale. An electric permittivity ratio of $\varepsilon_r = 0.6$ and the IL layer molarity of $M = 0.1$ mmol/L ($k^{-1} = 3.43$ nm) are constant. The IL−PD interfaces is subject to a much higher

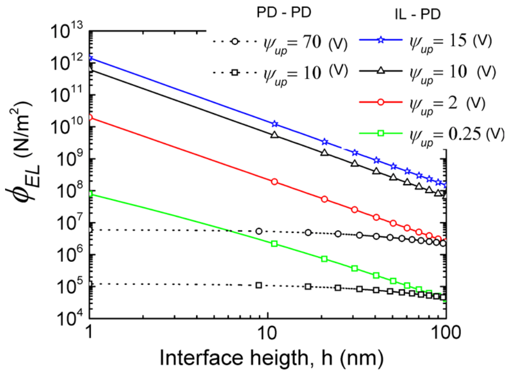

Figure 4. Electrostatic pressure variations versus interface height in PD−PD bilayer and IL−PD bilayer, considering applied potential effects. $M = 0.1$ mmol/L for IL−PD, $\varepsilon_1 = 2.5$ and $\varepsilon_2 = 4.17$.

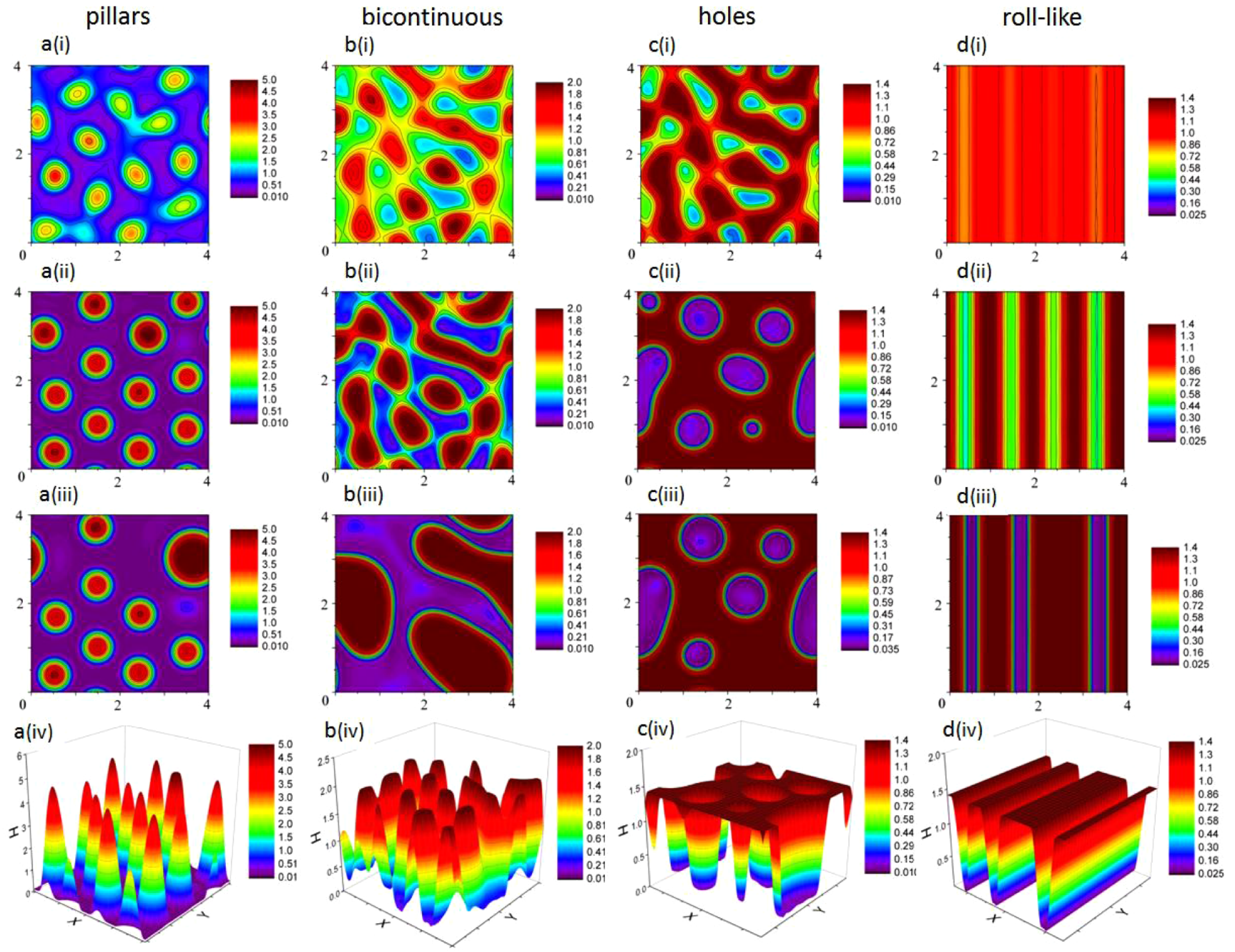

Figure 5. Base case PD–PD bilayer (a–d) images from i to iii show the 2-D spatiotemporal evolution for liquid–liquid interface instabilities in a $(4 \times 4)\lambda^2$ domain when $\varepsilon_r = 0.6$ and $\varepsilon_1 = 2.5$. Initial mean film thicknesses (h_0) are a(i-iv) 20 nm, b(i-iv) 50 nm, c(i-iv) 70 nm, and d(i-iv) 85 nm. Initial electric field intensities (E_0) are 294, 250, 227, and 212 MV/m, respectively. Nondimensional times for the 2-D plots are T = a(i) 9×10^4, a(ii) 3.4×10^5, and a(iii) 2.4×10^6; b(i) 8×10^2, b(ii) 1×10^3, and b(iii) 4×10^3; c(i) 2×10^2, c(ii) 6×10^2, and c(iii) 9×10^2; d(i) 1.8×10^3, d(ii) 2.2×10^3, and d(iii) 6.1×10^3. Plots a–d(iv) show 3-D snapshots of the liquid–liquid interface structure. Nondimensional times for the plots are T = a(iv) 3.4×10^5, b(iv) 1×10^3, c(iv) 6×10^2, and d(iv) 6.1×10^3.

electrostatic pressure compared with the PD–PD interface (in the order of 10^3 to 10^7 times higher for the ψ_{up} = 10 V case).

IL–PD bilayers are unstable under applied electric field while $\varepsilon_r < 1$. To investigate this response, PD–PD bilayers with $\varepsilon_r < 1$ are first considered by calculating the dynamics and resulting spatiotemporal evolution of interface. This provides a basis of comparison for unstable IL–PD bilayers in the next step.

Perfect Dielectric–Perfect Dielectric Bilayers (ε_r < 1). Bilayers with $\varepsilon_r < 1$, which act like perfect dielectric materials (i.e., there is no free charge or free ion in media) are examined first as a baseline for comparison to IL–PD bilayers. Electric breakdown in layers is not included in the simulations and it is assumed that the film layers behave like perfect dielectrics during the patterning process. The applied voltage, ψ_{up}, is set to a low value (20 V), but even at this low applied voltage, the expected electric field within the layers may exceed the dielectric field strength of the material and result in electric breakdown violating the model assumption.[39]

A 2-D spatiotemporal evolution and 3-D snapshots of the liquid–liquid interface instabilities for the homogeneous electric field and PD–PD bilayer with $\varepsilon_r = 0.6$ is shown in Figure 5. Initial mean film thicknesses (h_0) are a(i-iv) 20 nm, b(i-iv) 50 nm, c(i-iv) 70 nm, and d(i-iv) 85 nm. The electrostatic conjoining pressure pushes the interface downward, so some hollows in the lower layer are expected to form. Negative diffusion[29] moves the fluid from the thinner to the thicker region which assists in the growth of instabilities over time. Four distinct structures of the following: pillars a(iv), bicontinuous b(iv), holes c(iv), and roll-like d(iv) are observed. Similar to the bilayers with $\varepsilon_r > 1$,[29,41] pillars and bicontinuous structures form in PD–PD systems. However, holes and roll-like structures only form when there is a conjoining pressure for $\varepsilon_r < 1$.[27,30]

Pillars which have a hexagonal structure a(ii) imply that coalescence of the neighboring pillars a(iii) is due to their collision.[55] Bicontinuous structures, b(ii) and b(iii), behave like an air-in-liquid dispersion which occurs in air–polymer (i.e., monolayer) system with high filling ratios.[29] For hole formation the interface touches the upper electrode in the early stages of process, c(i), with dumbbell shape dents on the interface. These dents evolve into round shapes with time and deepen toward the lower electrode, c(ii). Compared to the pillars, a(ii), the holes, c(ii), do not have a hexagonal order over the domain; therefore, Ostwald ripening[55] is one possible reason for the coalescence of neighbor holes over time. Roll-like or straight groove-type structures seem to be an organized form of the bicontinuous structures generated by the same phase inversion mechanism.

Images a–d(ii) show the quasi-equilibrium structures and a–d(iii) are snapshots for the coalescence stage. The time that patterns remain in the quasi-equilibrium condition depends on physical parameters of the system like viscosity, electric permittivity ratio of layers, and initial mean thickness.[29,41,55]

To characterize different morphological behaviors in bilayers with ε_r = 0.6 and different thicknesses, as shown in Figure 5, a systematic numerical investigation is performed. A parametric map that captures the liquid–liquid interface structure for wide ranges of relative electric permittivity ratios of layers, ε_r, and nondimensional initial mean film thickness, h_0/d, is shown in Figure 6. Both initial layer thickness and electric permittivity ratio are critical factors in the EHL process and can create different patterns on the film. When the lower layer is thicker than the upper layer, the final pattern is more sensitive to electric permittivity. Changing the electric permittivity ratio of the bilayers results in the interfaces having two to four different kinds of structure depending on the initial thicknesses of the layers. For example, in the case of ε_r = 1.5, pillars and bicontinuous structures will form when h_0/d = 0.2 and 0.5, respectively; but for ε_r = 0.3, pillars, bicontinuous, and hole structures are observed for h_0/d ratios of 0.35, 0.5, and 0.6, respectively. Moreover, the interface can have four distinct structures, namely, pillars, bicontinuous, hole, and roll-like where ε_r = 0.6 and h_0/d ratios of 0.2, 0.6, 0.7, and 0.85, respectively.

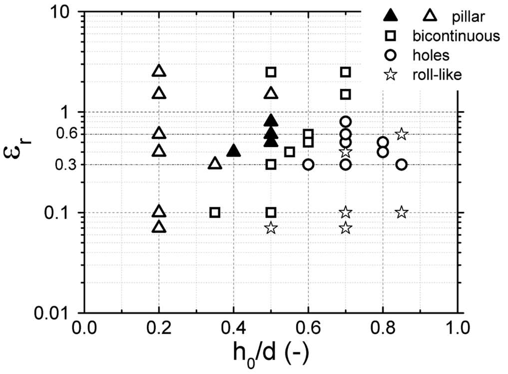

Figure 6. 2-D parametric map that illustrates the liquid–liquid interface structure as a function relative electric permittivity ratios of layers, ε_r, and nondimensional initial mean film thickness, h_0/d.

From a thermodynamic point of view, the final structure in the pattern formation process is the shape that is at the lowest Helmholtz free energy of the system which is in a thermodynamically stable state condition. In Figure 6, a critical initial film thickness for each ε_r can be found such that the EHD patterning process of films with initial thicknesses below this critical value results in pillar formation. The critical film thickness is called the Maxwell point[17,30] which is the inflection point in the plot of conjoining/disjoining pressure versus interface height in the steady state solution.[30] Varying the relative electric permittivity ratio of the layers changes the conjoining/disjoining pressure (see Figure 3) which results in a shift to the critical film thickness value.

In some cases, structures do not last for a long time, particularly for patterns that are close to the boundaries between different structures in Figure 6. Filled triangles in Figure 6 denote the unstable pillars which coalesce quickly and form bicontinuous structures. These are bounded between stable

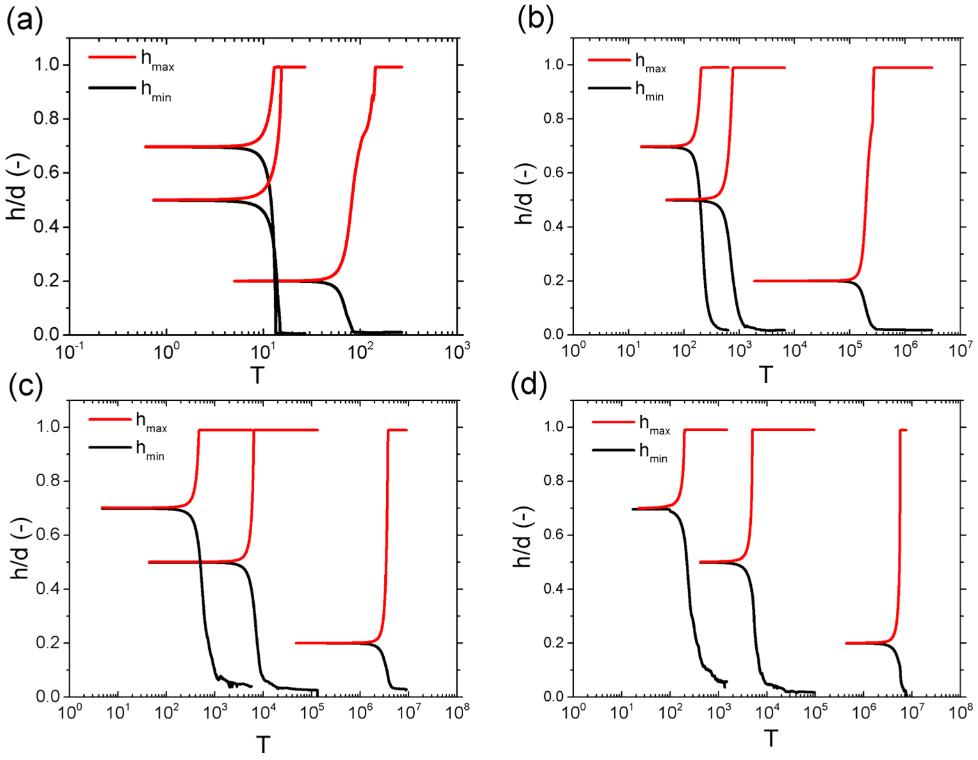

Figure 7. Nondimensional maximum and minimum film thickness, h/d (−), variations versus nondimensional time, T. Relative electric permittivity ratios of layers, ε_r, and initial mean film thickness, h_0, effects on the drainage time. Permittivity ratios are ε_r = (a) 0.1, (b) 0.6, (c) 1.5, and (d) 2.5. Initial electric field intensities (E_0) for 20-, 50-, and 70-nm-thick films are (a) 714, 363, and 273 MV/m; (b) 294, 250, and 227 MV/m; (c) 142, 160, and 174 MV/m; and (d) 90, 114, and 137 MV/m, respectively.

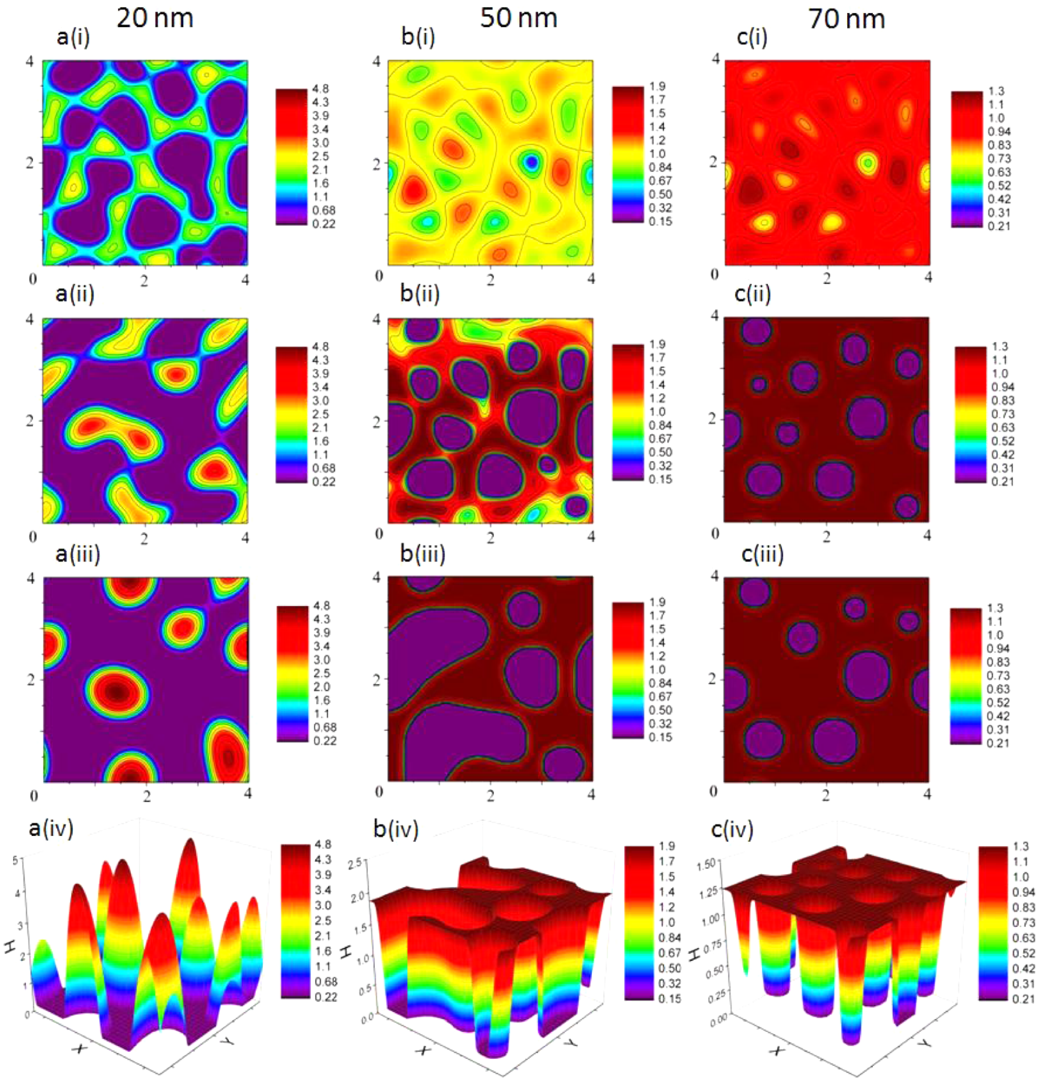

Figure 8. IL−PD bilayer (a−c) images from i to iii show the 2-D spatiotemporal evolution for liquid−liquid interface instabilities in a $(4 \times 4)\lambda^2$ domain when $\varepsilon_r = 0.6$ and M = 100 (mmol/L). Initial mean film thicknesses (h_0) are a(i-iv) 20 nm, b(i-iv) 50 nm, and c(i-iv) 70 nm. Nondimensional times for the plots are T = a(i) 9, a(ii) 11, and a(iii) 13.5; b(i) 7, b(ii) 8, and b(iii) 20; c(i) 7, c(ii) 10, and c(iii) 17. Plots a−c(iv) show 3-D snapshots of the liquid−liquid interface structure. Nondimensional times for the 3-D plots are T = a(iv) 13.5, b(iv) 20, and c(iv) 10. Initial electric field intensities (E_0) are (a) 90, (b) 11, and (c) 137 MV/m.

pillars and bicontinuous structures. By careful examination of Figure 6, it is found that as the mean initial thickness of the layers is varied (h_0/d), more types of structures are produced when $\varepsilon_r < 1$ is compared to $\varepsilon_r > 1$.

The effect of relative electric permittivity ratios of layers, ε_r, on the nondimensional maximum and minimum film thicknesses, h_{max}/d and h_{min}/d, over nondimensional time, T, for three polymer film thicknesses of 20, 50, and 70 nm is shown in Figure 7. Four values of (a) 0.1, (b) 0.6, (c) 1.5, and (d) 2.5 are chosen for the ε_r to compare the bilayer behavior for $\varepsilon_r > 1$ and $\varepsilon_r < 1$. The parameter h_{min} indicates when the lower layer drains (or nonwets the lower electrode) and h_{max} indicates when the lower layer touches the upper electrode in the domain. To compare bilayers with different thicknesses, interface height, h, is nondimensionalized using electrode distance as a length scale. The actual time in real experiments depends on the properties of the applied materials, mainly viscosity.[55] For bilayers with $\varepsilon_r < 1$, thicker films drain more rapidly than thinner ones as shown in Figure 7a,b, a similar trend is found for the bilayers with $\varepsilon_r > 1$ shown in Figure 7c,d.

Ionic Liquid−Perfect Dielectric Bilayers ($\varepsilon_r < 1$). When IL−PD bilayers are considered, it was found that the interface experiences higher electric field. The electrostatic model and corresponding electrostatic pressure derived earlier are used in the thin film equation to examine the spatiotemporal evolution of IL−PD interface. The electric permittivity ratio of bilayer is set to $\varepsilon_r = 0.6$, and the other physical parameters are kept the same as those of PD−PD bilayers for comparison purpose. Three bilayers with initial mean lower layer thicknesses (h_0) of 20, 50, and 70 nm are simulated and the 2-D spatiotemporal evolution and 3-D snapshots are shown in Figure 8.

For the IL−PD cases in Figure 8, a homogeneous electric field is applied in a $(4 \times 4)\lambda^2$ domain at $\varepsilon_r = 0.6$ and M = 100 mM/L. In the IL−PD case with a 20 nm lower layer initial thickness (Figure 8a), pillars form on the interface similar to the PD−PD system (Figure 5a). However, the generated pillars are more sparsely spread and have an elliptical cross section instead of circular. Increasing h_0 to 50 nm causes the IL−PD to switch to polydisperse holes (Figure 8b(ii). In the PD−PD bilayer a bicontinuous structure (Figure 5b(ii)) is formed at h_0 = 50 nm,

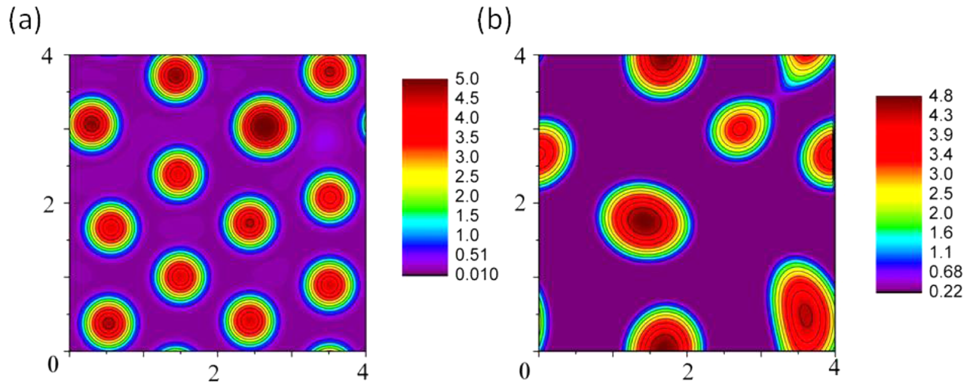

Figure 9. 2-D spatiotemporal evolution for liquid–liquid interface instabilities for the homogeneous electric field in (a) PD–PD and (b) IL–PD bilayers, in a $(4 \times 4)\lambda^2$ domain when $\varepsilon_r = 0.6$ and M = 100 (mmol/L) for the IL–PD bilayer. The initial mean film thickness is $h_0 = 20$ nm and the nondimensional times for the plots are T = (a) 3.4×10^5 and (b) 13.5. $\psi_{\text{up}} = 20$ V and initial electric field intensities (E_0) are (a) 294 and (b) 995.

which is unlike the similar condition IL–PD bilayer holes (Figure 8b(ii)). A further increase in h_0 to 70 nm in the IL–PD case leads to the generation of more organized holes (Figure 8c(ii)). Thus, using an ionic liquid in place of a perfect dielectric seems to effectively causes a shift to the left in the boundaries between structure types in Figure 6.

The disordered and polydispersed pillars of the IL–PD system which are captured in the numerical simulation are also experimentally observed.[39] Thus, the numerical simulation developed here in predicting the interface behavior in the IL–PD system seems to capture the dynamics of interest. A 2-D spatiotemporal evolution for liquid–liquid interface instabilities for the homogeneous electric field in (a) PD–PD and (b) IL–PD bilayers are directly compared in Figure 9. The number of pillars in the IL–PD bilayer is more than what is immediately apparent in Figure 9, since the physical domain size in IL–PD is 10 times less than that in PD–PD. Specifically, the average center-to-center distance of pillars is 210 nm for the IL–PD bilayer compared to 1336 nm for the PD–PD bilayer, quantifying the smaller size features in the IL–PD bilayers for this case.

■ CONCLUSIONS

Electrostatic force is used as a destabilizing external force to study the dynamics, morphological evolution, and drainage time of thin liquid bilayers (<100 nm). Due to the geometrical properties of the system (small aspect ratio of mean film thickness to lateral domain) a long-wave asymptotic theory is employed to simplify the coupled mass and momentum equations. This results in a nonlinear thin film equation approximation which is numerically solved. The generated thin film fluid structures of IL–PD bilayers for varying parameters are simulated and compared to the well-known PD–PD base case.

In PD–PD bilayers with $\varepsilon_r < 1$, pillar, bicontinuous, hole, and roll-like structures are formed, whereas the last two features are not observed in the bilayers with $\varepsilon_r > 1$. When the thin film is thicker than bounding media, the final pattern is more sensitive to the electric permittivity ratio. Thicker films are found to drain more rapidly in bilayers with $\varepsilon_r < 1$ similar to bilayers with $\varepsilon_r > 1$.

For IL–PD bilayers, to predict the electrostatic component of conjoining/disjoining pressure acting on the interface, an analytical model is developed based on the nonlinear Poisson-Boltzmann equation. Perfect dielectrics and perfect conductors are found as limiting cases for ionic liquids with low and high ionic strength, respectively. The IL–PD interface is subject to a much higher electrostatic pressure compared with the PD–PD interface (on the order of 10^3 to 10^7 times higher for the $\psi_{\text{up}} = 10$ V case). It is found that the IL–PD bilayers with $\varepsilon_r > 1$ remain stable under the action of transverse electric field, whereas similar PD–PD bilayers are unstable.

The use of an IL layer is found to reduce the size of the structures by a factor of ten ($\lambda_{\text{PD–PD}}$ is about ten times larger than $\lambda_{\text{IL–PD}}$) for the case studied. This has important implications when the goal is to produce small structures. The IL–PD pillars tend to be polydispersed and more disordered over the domain compared to the PD–PD ones. The developed analytical models and resulting numerical simulation closely predict the interface behavior for both PD–PD and IL–PD bilayers over the range of parameters tested when compared to other numerical studies and experimental observations in the literature. This indicates that the numerical simulation developed is of utility in predicting PD–PD and IL–PD bilayer responses to an applied electric field.

■ AUTHOR INFORMATION

Corresponding Author

*E-mail: bob.koch@ualberta.ca.

Notes

The authors declare no competing financial interest.

■ ACKNOWLEDGMENTS

We acknowledge financial support from the Natural Sciences and Engineering Research Council (NSERC), Canada, Chair in Water Quality Management for Oil Sands Extraction, the Alberta Water Research Institute (AWRI), Kemira, Outotec, Suncor Energy, Statoil and ConocoPhilips.

■ REFERENCES

(1) Quere, D. Fluid Coating on a Fiber. *Annu. Rev. Fluid Mech.* **1999**, *31*, 347–384.

(2) Eow, J. S.; Ghadiri, M.; Sharif, A. O.; Williams, T. J. Electrostatic Enhancement of Coalescence of Water Droplets in Oil: A Review of the Current Understanding. *Chem. Eng. J.* **2001**, *84*, 173–192.

(3) Mostowfi, F.; Khristov, K.; Czarnecki, J.; Masliyah, J.; Bhattacharjee, S. Electric Field Mediated Breakdown of Thin Liquid Films Separating Microscopic Emulsion Droplets. *Appl. Phys. Lett.* **2007**, *90*, 184102.

(4) Lin, S.; Brenner, H. Marangoni Convection in a Tear Film. *J. Colloid Interface Sci.* **1982**, *85*, 59–65.

(5) Vrij, A. Possible Mechanism for the Spontaneous Rupture of Thin Free Liquid Films. *Discuss. Faraday Soc.* **1966**, *42*, 23–33.

(6) Sheludko, A. Thin Liquid Films. *Adv. Colloid Interface Sci.* **1967**, *1*, 391−464.

(7) Ruckenstein, E.; Jain, R. K. Spontaneous Rupture of Thin Liquid Films. *J. Chem. Soc., Faraday Trans.* **1974**, *70*, 132−147.

(8) Williams, M. B.; Davis, S. H. Nonlinear Theory of Film Rupture. *J. Colloid Interface Sci.* **1982**, *90*, 220−228.

(9) Sharma, A. Relation of Thin Film Stability and Morphology to Macroscopic Parameters of Wetting in the Apolar and Polar Systems. *Langmuir* **1993**, *9*, 861−869.

(10) Oron, A.; Davis, S. H.; Bankoff, S. G. Long-Scale Evolution of Thin Liquid Films. *Rev. Mod. Phys.* **1997**, *69*, 931−980.

(11) A. Ghatak, R. K.; Sharma, A. Dynamics and Morphology of Holes in Dewetting of Thin Films. *J. Colloid Interface Sci.* **1999**, *212*, 483−494.

(12) Sharma, A.; Khanna, R. Pattern Formation in Unstable Thin Liquid Films Under the Influence of Antagonistic Short- and Long-range Forces. *J. Chem. Phys.* **1999**, *110*, 4929−4936.

(13) Chan, D. Y. C.; Klaseboer, E.; Manica, R. Film Drainage and Coalescence Between Deformable Drops and Bubbles. *Soft Matter* **2011**, *7*, 2235−2264.

(14) Sharma, A.; Ruckenstein, E. An Analytical Nonlinear Theory of Thin Film Rupture and Its Application to Wetting Films. *J. Colloid Interface Sci.* **1986**, *113*, 456−479.

(15) Mitlin, V. S. Dewetting of Solid Surface: Analogy with Spinodal Decomposition. *J. Colloid Interface Sci.* **1993**, *156*, 491−497.

(16) Schaffer, E.; Thurn-Albrecht, T.; Russell, T. P.; Steiner, U. Electrically Induced Structure Formation and Pattern Transfer. *Nature* **2000**, *403*, 874−877.

(17) Bestehorn, M.; Pototsky, A.; Thiele, U. 3D Large Scale Marangoni Convection in Liquid Films. *Eur. Phys. J. B* **2003**, *33*, 457−467.

(18) Schaffer, E.; Harkema, S.; Roerdink, M.; Blossey, R.; Steiner, U. Morphological Instability of a Confined Polymer Film in a Thermal Gradients. *Macromolecules* **2003**, *36*, 1645−1655.

(19) Wang, Q.; Zhang, L.; Zhao, X. Creasing to Cratering Instability in Polymers under Ultrahigh Electric Fields. *Phys. Rev. Lett.* **2011**, *106*, 118301.

(20) Corbett, A.; Kumar, S. Combined Thermal and Electrohydrodynamic Patterning of Thin Liquid Films. *J. Eng. Math.* **2013**, 1−16.

(21) Trice, J.; Favazza, C.; Thomas, D.; Garcia, H.; Kalyanaraman, R.; Sureshkumar, R. Novel Self-Organization Mechanism in Ultrathin Liquid Films: Theory and Experiment. *Phys. Rev. Lett.* **2008**, *101*, 017802.

(22) Krishna, H.; Shirato, N.; Yadavali, S.; Sachan, R.; Strader, J.; Kalyanaraman, R. Self-Organization of Nanoscale Multilayer Liquid Metal Films: Experiment and Theory. *ACS Nano* **2011**, *5*, 470−476.

(23) Berendsen, C. W. J.; Zeegers, J. C. H.; Darhuber, A. A. Thinning and Rupture of Liquid Films by Moving Slot Jets. *Langmuir* **2013**, *29*, 15851−15858.

(24) Khanna, R.; Sharma, A. Pattern Formation in Spontaneous Dewetting of Thin Apolar Films. *J. Colloid Interface Sci.* **1997**, *195*, 42−50.

(25) Israelachvili, J. N. *Intermolecular and Surface Forces*; Academic Press: Burlington, MA, 2011.

(26) Masliyah, J. H.; Bhattacharjee, S. *Electrokinetic and Colloid Transport Phenomena*; Wiley-Interscience: Hoboken, NJ, 2006.

(27) Lin, Z.; Kerle, T.; Russell, T. P.; Schäffer, E.; Steiner, U. Structure Formation at the Interface of Liquid/Liquid Bilayer in Electric Field. *Macromolecules* **2002**, *35*, 3971−3976.

(28) Salac, D.; Wei, L.; Chia-Wei, W.; Sastry, A. M. Pattern Formation in a Polymer Thin Film Induced by an In-plane Electric Field. *Appl. Phys. Lett.* **2004**, *85*, 1161−1163.

(29) Verma, R.; Sharma, A.; Kargupta, K.; Bhaumik, J. Electric Field Induced Instability and Pattern Formation in Thin Liquid Films. *Langmuir* **2005**, *21*, 3710−3721.

(30) Wu, N.; Russel, W. B. Electrohydrodynamic Instability of Dielectric Bilayers: Kinetics and Thermodynamics. *Ind. Eng. Chem. Res.* **2006**, *45*, 5455−5465.

(31) Kim, D.; Lu, W. Three-Dimensional Model of Electrostatically Induced Pattern Formation in Thin Polymer Films. *Phys. Rev. B* **2006**, *73*, 35206.

(32) Wu, N.; Russel, W. B. Micro- and Nano-patterns Created via Electrohydrodynamic Instabilities. *Nano Today* **2009**, *4*, 180−192.

(33) Voicu, N. E.; Harkema, S.; Steiner, U. Electric-Field-Induced Pattern Morphologies in Thin Liquid Films. *Adv. Funct. Mater.* **2006**, *16*, 926−934.

(34) Verma, R.; Sharma, A.; Banerjee, I.; Kargupta, K. Spinodal Instability and Pattern Formation in Thin Liquid Films Confined Between Two Plates. *J. Colloid Interface Sci.* **2006**, *296*, 220−232.

(35) Bae, J.; Glogowski, E.; Gupta, S.; Chen, W.; Emrick, T.; Russell, T. P. Effect of Nanoparticles on the Electrohydrodynamic Instabilities of Polymer/Nanoparticle Thin Films. *Macromolecules* **2008**, *41*, 2722−2726.

(36) Roberts, S. A.; Kumar, S. AC Electrohydrodynamic Instabilities in Thin Liquid Films. *J. Fluid Mech.* **2009**, *631*, 255−279.

(37) Roberts, S. A.; Kumar, S. Electrohydrodynamic Instabilities in Thin Liquid Trilayer Films. *Phys. Fluids* **2010**, *22*, 122102.

(38) Reddy, P. D. S.; Bandyopadhyay, D.; Sharma, A. Self-Organized Ordered Arrays of Core-Shell Columns in Viscous Bilayers Formed by Spatially Varying Electric Fields. *J. Phys. Chem. C* **2010**, *114*, 21020−21028.

(39) Lau, C. Y.; Russel, W. B. Fundamental Limitations on Ordered Electrohydrodynamic Patterning. *Macromolecules* **2011**, *44*, 7746−7751.

(40) Gambhire, P.; Thaokar, R. Linear Stability Analysis of Electrohydrodynamic Instabilities at Fluid Interfaces in the Small Feature Limit. *Eur. Phys. J. E* **2011**, *34*, 1−12.

(41) Atta, A.; Crawford, D. G.; Koch, C. R.; Bhattacharjee, S. Influence of Electrostatic and Chemical Heterogeneity on the Electric-Field-Induced Destabilization of Thin Liquid Films. *Langmuir* **2011**, *27*, 12472−12485.

(42) Gambhire, P.; Thaokar, R. M. Role of Conductivity in the Electrohydrodynamic Patterning of Air-Liquid Interfaces. *Phys. Rev. E* **2012**, *86*, 036301.

(43) Wang, Q.; Zhao, X. Creasing-Wrinkling Transition in Elastomer Films under Electric Fields. *Phys. Rev. E* **2013**, *88*, 042403.

(44) Mondal, K.; Kumar, P.; Bandyopadhyay, D. Electric Field Induced Instabilities of Thin Leaky Bilayers: Pathways to Unique Morphologies and Miniaturization. *J. Chem. Phys.* **2013**, *138*, 024705.

(45) Roy, S.; Biswas, D.; Salunke, N.; Das, A.; Vutukuri, P.; Singh, R.; Mukherjee, R. Control of Morphology in Pattern Directed Dewetting of a Thin Polymer Bilayer. *Macromolecules* **2013**, *46*, 935−948.

(46) Benney, D. J. Long Waves on Liquid Films. *J. Math. Phys.* **1966**, *45*, 150−155.

(47) Yang, Q.; Li, B. Q.; Ding, Y. Dynamic Modelling of Micro/Nano-patterning Transfer by an Electric Field. *RSC Adv.* **2013**, *3*, 24658−24663.

(48) Yang, Q.; Li, B. Q.; Ding, Y. A Numerical Study of Nanoscale Electrohydrodynamic Patterning in a Liquid Film. *Soft Matter* **2013**, *9*, 3412−3423.

(49) Saville, D. A. Electrohydrodynamics: The Taylor-Melcher Leaky Dielectric Model. *Annu. Rev. Fluid Mech.* **1997**, 27−64.

(50) Craster, R. V.; Matar, O. K. Electrically Induced Pattern Formation in Thin Leaky Dielectric Films. *Physics of Fluids (1994-present)* **2005**, *17*, 1131−1198.

(51) Gambhire, P.; Thaokar, R. Electrokinetic Model for Electric-Field-Induced Interfacial Instabilities. *Phys. Rev. E* **2014**, *89*, 032409.

(52) Lee, D. W.; Im, D. J.; Kang, I. S. Electric Double Layer at the Interface of Ionic Liquid-Dielectric Liquid under Electric Field. *Langmuir* **2013**, *29*, 1875−1884.

(53) Atherton, R. W.; Homsy, G. M. On the Derivation of Evolution Equations for Interfacial Waves. *Chem. Eng. Commun.* **1976**, *2*, 57−77.

(54) Sharma, A.; Khanna, R. Pattern Formation in Unstable Thin Liquid Films. *Phys. Rev. Lett.* **1998**, *81* (16), 3463−3466.

(55) Wu, N.; Kavousanakis, M. E.; Russel, W. B. Coarsening in the Electrohydrodynamic Patterning of Thin Polymer Films. *Phys. Rev. E* **2010**, *81*, 26306.

(56) Landau, L. D.; Lifshitz, E. M. *Electrodynamics of continuous media*; Pergamon Press, 1960.

(57) Bandyopadhyay, D.; Sharma, A.; Thiele, U.; Reddy, P. D. S. Electric-Field-Induced Interfacial Instabilities and Morphologies of Thin Viscous and Elastic Bilayers. *Langmuir* **2009**, *25*, 9108−9118.

(58) Brenan, K. E.; Petzold, L. R. The Numerical Solution of Higher Index Differential/Algebraic Equations by Implicit Methods. *SIAM J. Numer. Anal.* **1989**, *26* (4), 976−996.

(59) Dickey, M. D.; Gupta, S.; Leach, K. A.; Collister, E.; Willson, C. G.; Russell, T. P. Novel 3-D Structures in Polymer Films by Coupling External and Internal Fields. *Langmuir* **2006**, *22*, 4315−4318.

(60) Morariu, M. D.; Voicu, N. E.; Schaffer, E.; Lin, Z.; Russell, T. P.; Steiner, U. Hierarchical Structure Formation and Pattern Replication Induced by an Electric Field. *Nat. Mater.* **2003**, *2*, 48−52.